AIChE

Numerical Study of Solid–Liquid Fluidization Dynamics

Frédéric Gevrin, and Olivier Masbernat
Université de Toulouse, INPT-UP, Laboratoire de Génie Chimique, 31432 Toulouse, France; and CNRS, FERMaT FR 3089, Allée E. Monso 31432 Toulouse, France

Olivier Simonin
Université de Toulouse, INPT-UPS, Institut de Mécanique des Fluides de Toulouse, 31400 Toulouse, France; and CNRS, FERMaT FR 3089, Allée E. Monso, 31432 Toulouse, France

DOI 10.1002/aic.12209
Published online May 24, 2010 in Wiley Online Library (wileyonlinelibrary.com).

A numerical model based on the kinetic theory of granular media has been tested to simulate the unsteady two-phase flow in solid–liquid fluidized beds. We focus here on the local unsteady flow features as predicted by the model and comparison with experimental data of Zenit and Hunt (2000) are discussed. In most of the cases, a series of two-dimensional rotational structures develops along the bed height, which controls the instantaneous solid fraction field as well as the level of fluctuating kinetic energy of the particles. Interestingly, with high inertia particles and at high solid concentration, these structures disappear to the benefit of a one-dimensional oscillating flow. The shape of these concentration waves is very similar to those previously observed by Nicolas et al. (1999) and Duru et al. (2002). The solid fraction density spectrum and variance have been analyzed and compared with the experimental data of Zenit and Hunt. © 2010 American Institute of Chemical Engineers *AIChE J,* 56: 2781–2794, 2010
Keywords: fluidization, fluid mechanics, multiphase flow, particulate flows

Introduction

Despite its minor importance as an industrial process compared with gas fluidization, liquid fluidization applications cover a wide range of mass or heat transfer operations, crystallization, or catalytic reactions, and liquid fluidized beds are commonly used as growth biochemical reactors in wastewater treatment.[1] The scaling and control of such bioreactors require the detailed knowledge of particle–fluid and particle–particle interactions at a fine scale, to correctly predict as an example bio-film growth and detachment rates.[2]

On the other hand, liquid fluidization is an academic test case of interest in view of evaluating two-phase flow modeling. Even if it does not engender intense chaotic flows such as bubbling phenomenon in gas–particle fluidization, solid–liquid fluidized bed cannot be considered as homogeneous dispersed flow over a wide range of length scales.[3] In particular, large scale, low-frequency concentration fluctuations have been experimentally observed in liquid fluidized beds. The characteristics (length and time scales) of these fluctuations and the transition between the different regimes detected (wavy, turbulent, or ''bubbly'') are strongly related to the ratio between the fluidization velocity to the minimum fluidization velocity for a given particle–fluid system.[4] A number of studies has been devoted to the understanding and the characterization of concentration waves in liquid fluidized beds,[5] with the idea in mind that the bubbling regime in gas–particle beds originates from the same kind of instability.[6–8] The prediction of the liquid fluidized bed microstructures and macrostructures, therefore, implies an unsteady

Correspondence concerning this article should be addressed to O. Masbernat at olivier.masbernat@ensiacet.fr.

formulation of the two-phase motion governing equations. The two-phase modeling of solid–liquid fluidized beds has focused the interest of researchers for four decades till date with the pioneer works of Jackson,[9] Murray,[10] and Anderson and Jackson.[11] In the frame of eulerian averaged models, the literature exhibit two distinct model families, the classical two-fluid models (volume or phase averaged models) and statistical models derived from kinetic theory of granular media, both of these approaches leading to similar expressions for the mass and momentum equations. The main difference between these two approaches lies in the treatment of the particle phase, which stress tensor reads[12,13]

$$\sum_{\mathrm{p},ij} = \left[P_\mathrm{p} - \lambda_\mathrm{p}\nabla.\mathbf{U}_\mathrm{p}\right]\mathbf{I} - \mu_\mathrm{p}\left[\nabla\mathbf{U}_\mathrm{p} + {}^{\mathrm{t}}\nabla\mathbf{U}_\mathrm{p} - 2/3\nabla.\mathbf{U}_\mathrm{p}\mathbf{I}\right] \tag{1}$$

where P_p, λ_p, and μ_p are the dispersed phase (granular) pressure, volume, and shear viscosities, respectively. $\mathbf{U}_\mathrm{p}$ is the particle phase velocity vector averaged over the small scale fluctuating motion. Note that unlike single phase incompressible flows, because of mass conservation, the velocity divergence $\bigtriangledown.\mathbf{U}_\mathrm{p}$, cannot be disregarded in Eq. 1.

In the first kind of model, closure laws need to be established for the stress tensor of the dispersed phase, which is generally done on the basis of semiempirical approaches,[14,15] or experimental data.[8] Following this model, only first order closure laws can be accounted for with concentrated media and they are restricted to the particular case of fluidization. Indeed, for a given fluid–particle system, the only scaling parameter in a fluidized bed is the global solid fraction φ_p and all the macroscopic quantities such as the slip velocity, the particle velocity fluctuations (granular temperature), the dispersed phase (granular) pressure, or viscosities are explicit functions of φ_p.

In the second kind of model, the expression of the dispersed phase stress tensor naturally derives from the integration of Maxwell–Boltzmann equation of the particle velocity pdf.[12,16] The rate of change of particle momentum resulting from this integration includes both interactions with the surrounding fluid (Newton's equation) and particle–particle interactions through binary collisions. Analytical forms of the collision operator are obtained using kinetic theory of nonuniform gases[17] extended to the case of concentrated media.[16] Moreover, with this approach, the granular pressure and viscosities are explicitly related to the particle random motion, whose transport equations are derived from integration of second order moment weighted velocity pdf equations. Note, however, that such a modeling supposes that particle–particle interactions only result from collisions and neglects local hydrodynamic interactions, which a priori limits its application to the description of fluid–particle flow with large density ratio such as gas–particle flows at high concentration.[13,18–21] Then, using a formalism based on a joint fluid–particle velocity pdf kinetic equation, such an approach was extended to dispersed turbulent two-phase flows for particles with diameter that are very small compared with the energetic eddy length scales of the carrier flow turbulence.[22–25] In a former work, a statistical two-phase model based on the kinetic theory of granular media has been applied to solid–liquid fluidization.[26,27] Despite the fundamental difference between collisions and hydrodynamic interactions, its extension to the modeling of solid–liquid fluidization can find some a priori justification based on the following arguments: first, it must be pointed out that the form of the constitutive laws describing the particle phase rheology (Eq. 1) with both kinds of models (volume averaged and kinetic theory of granular media) are very similar, except that there is no physically unknown coefficient in the statistical model. Second, the model used in that study accounts for the interstitial fluid influence on the particle motion via the drag force in the momentum equation as well as in the fluctuating kinetic energy of the particles, q_p^2. In particular, the time scales of the dispersed phase kinetic viscosity and of the dissipation rate of q_p^2 result from the competition between the characteristic relaxation time of the particles and the time between two successive collisions. This model has been tested against the experimental data of Zenit et al.[28] for three types of particle fluidized by water with contrasted inertia (characterized by the particle Stokes number) and in a wide range of global solid fraction, φ_p. The evaluation of the model was discussed on the basis of the comparison between the experimental values of the granular pressure (measured with the help of a piezo-electric probe at the wall) and the predicted values. The results showed a good level of agreement, the best prediction level being observed with the most inertial particles.[26] In this work, we focus on the unsteady features of the fluidized bed as calculated by the model for the same experimental conditions (particles and phase fraction) as those studied by Zenit and Hunt.[29] The discussion also addresses other experimental findings related to concentration wave propagation analysis.[7,8]

Transport of Particle Fluctuations

We recall in the following the outlines of the statistical model used in this work. Continuity and momentum equations in both phases take the classical form as that derived in unsteady two-fluid models, with an interfacial momentum transfer term accounting for the drag force only (inertia forces such as added mass have little effect in this application). The contribution of proper turbulence of the continuous phase modeled in the frame of the joint fluid particle pdf approach assuming very small particle diameter with respect to the energetic turbulent eddy length scale is found negligible. This results from the fact that, according to the modeling approach, in a solid–liquid fluidized bed (for a global solid phase fraction $\varphi_\mathrm{p} > 0.1$), the turbulence produced by the macroscopic velocity gradients of the continuous phase is damped by the fluid–particle interaction. However, we must notice that the model neglect the influence of the velocity fluctuations (pseudoturbulence) locally produced by the fluid–particle interaction, which are assumed to be at small scales with respect to the particle diameter and locally dissipated by fluid viscous effect.[25] Development of the particle stress tensor constitutive laws in Eq. 1 lead to the following expression for the granular pressure[12,13]:

$$P_\mathrm{p} = \frac{2}{3}\alpha_\mathrm{p}\rho_\mathrm{p}q_\mathrm{p}^2[1 + 2\alpha_\mathrm{p}g_0(1 + e_\mathrm{c})] \tag{2}$$

where α_p and ρ_p are the local solid phase fraction and density, respectively, and e_c is the normal coefficient of restitution. The RHS second term of Eq. 2 is the collisional contribution

accounting for finite volume effect of particles at high concentration through the hindering function g_0 (Enskog correction). This function is a growing function of the solid fraction α_p, which tends toward infinity at the maximum packing concentration $\alpha_{p,m}$. In this model, this function takes the form proposed by Lun and Savage[30]:

$$g_0 = \left(1 - \frac{\alpha_p}{\alpha_{p,m}}\right)^{-2.5\alpha_{p,m}} \tag{3}$$

The granular shear viscosity μ_p includes a kinetic and a collisional contribution given by[21]:

$$\nu_p^{kin} = \frac{2}{3\sigma_c}\tau_p^c q_p^2(1+\alpha_p g_0 \phi_c)\left(1 + \frac{2\tau_p^c}{\sigma_c T_{fp}^F}\right)^{-1} \tag{4}$$

$$\nu_p^{col} = \frac{4}{5}\alpha_p g_0(1+e_c)\left(\nu_p^{kin} + d\sqrt{\frac{2}{3}\frac{q_p^2}{\pi}}\right) \tag{5}$$

$$\mu_p = \alpha_p \rho_p \left(\nu_p^{kin} + \nu_p^{col}\right) \tag{6}$$

where φ_c and σ_c are analytical functions of e_c. τ_p^c and T_{fp}^F are the time between two successive collisions and the mean particle relaxation time due to the drag. Therefore, Eq. 4 shows that the kinetic viscosity time scale is controlled by the smallest time scale between τ_p^c and T_{fp}^F. T_{fp}^F is modeled following Wen and Yu's drag law[31]:

$$\frac{1}{T_{fp}^F} = \frac{(3\rho_f C_D)}{4\rho_p d}(1-\alpha_p)^{-1.7}|\overline{\mathbf{u}_r}| \tag{7}$$

where C_D is the particle drag coefficient deduced from the law of Schiller and Nauman (in Clift et al.[32]), and $\mathbf{u}_r$ is the local slip velocity:

$$C_D = \frac{24}{Re}(1+0.15Re^{0.687}) \text{with } Re = \frac{(1-\alpha_p)|\overline{\mathbf{u}_r}|d}{\nu_f} \tag{8}$$

The time between two successive collisions is given by[13]:

$$\tau_p^c = \sqrt{\frac{3\pi}{2}}\frac{d}{24\alpha_p g_0 \sqrt{q_p^2}} \tag{9}$$

In the limit of very dilute systems, the collision time scale τ_p^c may become very large. In that case, the time scale governing the kinetic viscosity in Eq. 4 is T_{fp}^F. The competition between these two time scales in the formulation of the kinetic viscosity represents one important difference with "dry" granular models.

From Eq. 5, it can also be deduced that at high phase fraction the granular viscosity will be dominated by its collisional part, ν_p^{col}. Finally, the expression of the volume viscosity λ_p reads[13]:

$$\lambda_p = \frac{4}{3}\alpha_p^2 \rho_p d g_0(1+e_c)\sqrt{\frac{2q_p^2}{3\pi}} \tag{10}$$

At high phase fraction, the volume viscosity will be as important as the collisional viscosity. All these constitutive laws (Eqs. 2–9) arise from the development of the collisional operator in the averaged Maxwell–Boltzmann velocity distribution. One basic assumption is that the velocity pdf of the agitated medium is not far from a Maxwellian distribution, so the anisotropy of the fluctuations is weak.[13,16] The rheology of the dispersed phase is then fully described and is related to the local fluctuating kinetic energy of the particles, q_p^2 (or granular temperature). It must be pointed out that because of this dependence between the solid phase viscosities and the fluctuating motion, the solid phase cannot be considered as a Newtonian fluid. Indeed, the granular temperature is related to the mean stress tensor in the transport equation of q_p^2, given by:

$$\alpha_p\rho_p\frac{Dq_p^2}{Dt} = \frac{\partial}{\partial x_i}\left(\alpha_2\rho_2(K_p^{kin}+K_p^{col})\frac{\partial q_p^2}{\partial x_i}\right) - \sum_{p,ij}\frac{\partial U_{p,j}}{\partial x_i} + 2\alpha_p^2\rho_p(1-e_c^2)g_0 q_p^2\frac{\partial U_{p,i}}{\partial x_i} - \alpha_p\rho_p\frac{2}{T_{fp}^F}q_p^2 - \alpha_p\rho_p\frac{(1-e_c^2)}{3\tau_p^c}q_p^2 \tag{11}$$

The first term of Eq. 11 RHS is the diffusive term which happened to have negligible weight in all simulations performed with the experimental test cases of Zenit et al. The second term is a source of production that includes compressibility effects (velocity divergence) via the granular pressure and the volume viscosity, and shear induced effects (velocity gradient) via the granular viscosity. These two distinct contributions arise from the development of the particle stress tensor (Eq. 1 in Eq. 11). The third term is a dissipative (hence, always negative in average) term associated to the compressibility of the solid phase. Finally, the fourth and fifth terms are the dissipation rates by the viscous drag and by the collisions, respectively.

Together with the continuity and momentum transport equations of both phases, Eqs. 1–11 build a closed set of equations that have been numerically solved in a two-dimensional (2D) domain. Details of the numerical method are given elsewhere.[26]

The domain and mesh size and the numerical values of the parameters used in the simulations are reported in Table 1.

The selected test cases of solid–liquid fluidization have been taken from the experimental flow parameters of Zenit et al.[28,29] and are reported in Table 2.

The particles have contrasted inertia but the same Richardson–Zaki exponent $n = 2.4$ (inertial regime):

$$U_0 = U_t(1-\varphi_p)^n \tag{12}$$

For a given fluidization velocity, the level of average fluctuating kinetic energy in the bed (hence of granular pressure) therefore varies considerably from the lightest particles to the heaviest, as shown in Gevrin et al.[26]

The main results of that study are summarized below.

A good agreement was observed between the measured and predicted granular pressure in the whole range of φ_p with the most inertial particles tested (steel beads, Figure 1), whereas with the nylon beads (lowest Stokes number), the

Table 1. Numerical Simulation Parameters

Bed height (m)	2.04
Bed width (m)	5.1×10^{-2}
Horizontal node number	11
Vertical node number	502
Horizontal mesh size (m)	5.1×10^{-3} (constant)
Vertical mesh size (m)	4×10^{-3} (constant)
Numerical time step (s)	1.5×10^{-3} (constant)
Elasticity coefficient e_c	0.9
Pair correlation function g_0	Lun and Savage (1986)
Liquid density (kg m^{-3})	1×10^3
Liquid viscosity (Pa s)	1×10^{-3}
Maximum packing concentration $\alpha_{p,m}$	0.64

present model overpredicts the experimental data, in particular at high solid phase fraction (above 0.3). Close to the maximum packing concentration, the abrupt decrease of the averaged granular pressure is reproduced only with the steel beads (Figure 1). It was also shown that such a quantity is weakly sensitive to the form of some constitutive laws used in the model equations (such as g_0 or ν_p^{kin}) and to the coefficient of restitution e_c, resulting from nonlinear interactions which tend to counterbalance any variation in these laws. Overall, the results can be judged satisfactory, considering the absence of real parameters in the model and the uncertainty associated with the measurements of the granular pressure, in particular at low Stokes number.[28] The corresponding evolution of q_p^2 as a function of φ_p is illustrated in Figure 2 in the case of steel beads. The curve passes through a maximum around $\varphi_p = 0.2$, a value which corresponds to that predicted by the semiempirical model of Batchelor.[14] As the solid fraction is increased, the production of q_p^2 is enhanced through collective effects (concentration and velocity gradients). The presence of this maximum originates from the decrease of the slip velocity and the increase of the interparticle collision rate which both tend to reduce the level of particle fluctuations. The simulated data can be modeled in all cases using a semiempirical scaling law (Figure 2):

$$\left\langle \overline{q_p^2} \right\rangle \propto U_t^2 \left[C_{D0} \varphi_p (1-\varphi_p)^{-4.7} \right]^{2/3} (1-\varphi_p/\varphi_{p,m})^{2n\varphi_{p,m}} \quad (13)$$

where C_{D0} is the Schiller and Nauman drag coefficient of a single particle based on the slip velocity U_0. Although quite simple under this form, the average level of q_p^2 in the bed results from different contributions in the production–dissipation budget. Indeed, the analysis of the time and space averaged transport equation of q_p^2 (Eq. 11) showed that in the general case,[26] the production of q_p^2 is mainly monitored by the mean velocity gradient of the dispersed phase and the dissipation by the viscous drag (fourth term of Eq. 11 RHS).

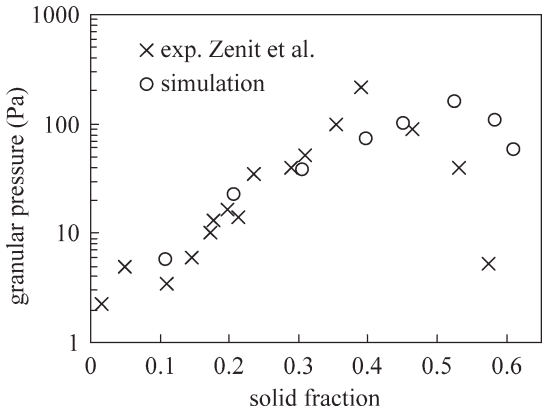

Figure 1. Granular pressure averaged in the bed as a function of averaged solid fraction for steel beads.

At high Stokes number (steel beads) and high concentration, however, compressibility effects via the granular pressure are responsible of the production mechanism and in this case, the major dissipation source is provided by the interparticle collisions (fifth term of Eq. 11 RHS).

Instantaneous Structure of Particle Hydrodynamic Field

Examination of the instantaneous structure of the particle flow and concentration fields is necessary to go further in the analysis and understanding of the model behavior. To illustrate it, the instantaneous large scale structures of the solid fraction α_p (left graph), the solid phase fluctuating kinetic energy q_p^2 (middle graph), and velocity fields of $\mathbf{U}_p$ (right graph) are displayed in Figures 3–5 for the three types of beads investigated at a low (Figures 3a, 4a, and 5a) and a high (Figures 3b, 4b, and 5b) global concentration (or, respectively, at a high and low fluidization velocity). To ease the reading of these graphs, the horizontal axis has been expanded.

As a first observation, the instantaneous distribution of the hydrodynamic variables is far from being uniform. At the lowest concentration studied, the existence of relative high gradients of solid fraction within the bed is noticeable with local values spanning one order of magnitude. In this case, the development of an axial gradient of particle concentration clearly appears, the lower part of the bed corresponding to a zone of lower concentration than the upper part. For the highest concentration, this vertical gradient is damped but still exists. The nonuniform structure of the particle concentration is characterized by either a succession of nearly horizontal stripes of high and low particle concentration or a

Table 2. Particle Properties (from Zenit et al.[28])

Beads	Diameter d (10^{-3} m)	D/d	ρ_p/ρ_f	U_t (m s^{-1})	Re_t	St	n
Nylon	6.35	8	1.14	0.136	785	7	2.4
Glass	3.00	17	2.54	0.318	2583	15	2.4
Steel	4.5	11.3	7.78	0.896	3665	47	2.4

Liquid phase is water at 20°C—Bed diameter $D = 5.1 \times 10^{-2}$ m.

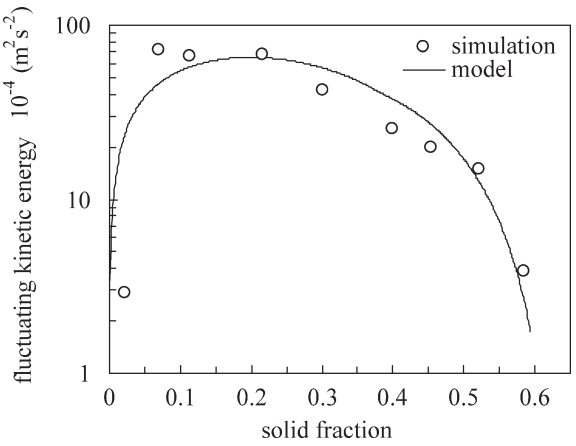

Figure 2. Fluctuating kinetic energy of the solid phase averaged in the bed as a function of averaged solid fraction for steel beads.

Continuous line corresponds to Eq. 13.

succession of concentric zones within which the solid fraction is decreasing from the periphery to the centre of these zones. At high concentration and with the nylon and glass beads (low and moderate inertia particles, respectively), the concentric zones tend to "coalesce," leading to a zigzag-like structure (Figures 3b and 4b).

These instantaneous organized structures of the particle concentration are consistent with the particle velocity and fluctuating energy fields. The concentric structure of the solid fraction field is associated to a succession of contra-rotating circulation loops of the velocity field along the bed height, which characteristic size compares with the column diameter. The instantaneous distribution of particles can then be explained as resulting from centrifugal effects within these loops. The correspondence with the instantaneous field of fluctuating energy is also remarkable, which often appears as the "negative" of the instantaneous picture of the concentration field. In fact, the location of q_p^2 maxima in the bed does correspond to the boundary between the circulating loops or equivalently to the location of the highest velocity gradients. This result confirms the former analysis of the production source terms in Eq. 11 with low inertia particles, which is controlled in this case by the mean velocity gradient.[26] In the case of highest inertia particles (steel beads) at high phase fraction (>40%), a train of planar concentration waves takes place along the bed height. This train consists of horizontal stripes of high solid fraction (close to the maximum packing fraction) followed by a layer of less concentrated particles (Figure 5b). Such a regime is associated with the predominance of compressibility effect (granular pressure) induced production terms in the fluctuating kinetic energy budget, as shown by Gevrin et al.[26]

Analysis of Solid Fraction Fluctuations

Time signal

Following the experimental study of Zenit and Hunt,[29] the time signal of the fluctuation of the solid fraction averaged over the bed cross section $\langle \alpha_p \rangle_S - \langle \overline{\alpha_p} \rangle_S$ (time average of this signal is zero) has been plotted at different heights along the fluidized bed. The axial evolution of this time signal at high concentration (close to 0.6) is reported in Figures 6–8 with the nylon, glass, and steel beads, respectively. Each of these signals is plotted over a 10-s period, which is larger than the largest characteristic time scale of the solid phase fraction fluctuations. In each test section of the bed, these signals are, therefore, the representatives of the whole time signal. As a first observation, the solid phase fraction fluctuation signal varies along the bed axis. For each type of bead, the development of low-frequency fluctuations from the bottom to the top of the bed can be observed. This evolution is more pronounced with the most inertial particles (steel beads). In this case, a concentration wave develops in

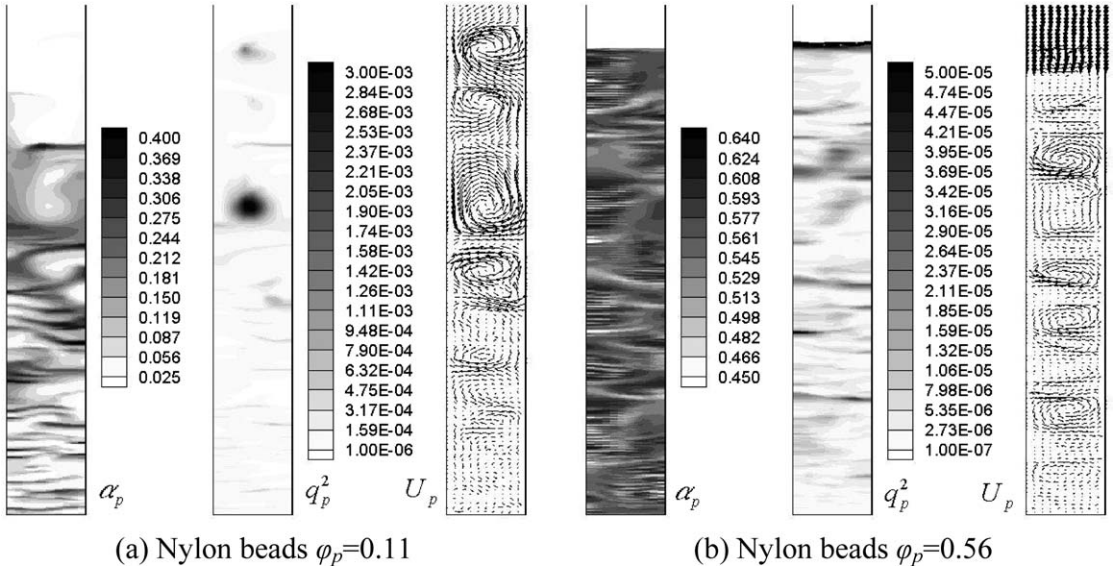

(a) Nylon beads φ_p=0.11 (b) Nylon beads φ_p=0.56

Figure 3. Instant fields of solid phase fraction, fluctuating kinetic energy, and velocity in the fluidized bed for Nylon beads (a) dilute regime (b) concentrated regime (Nylon beads).

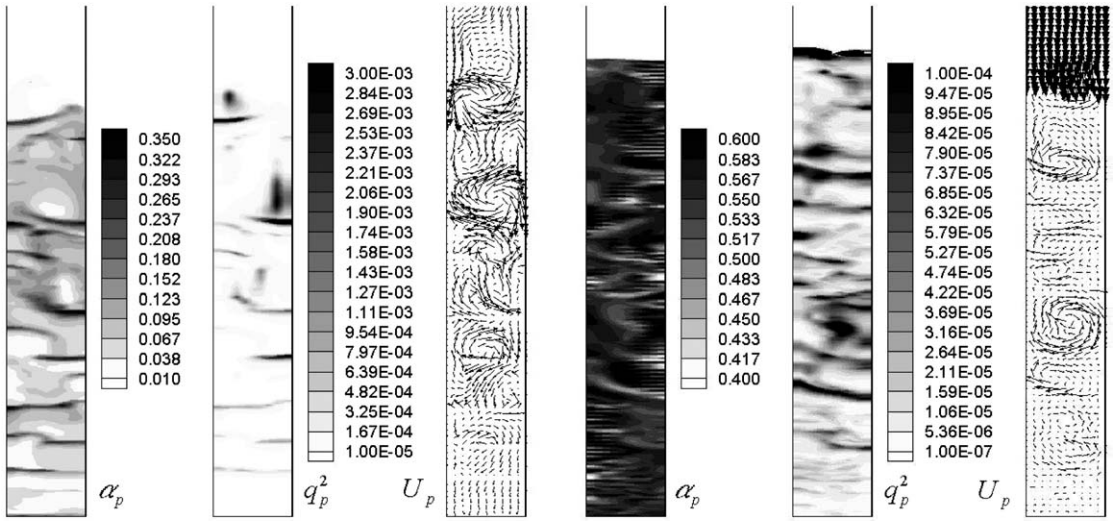

(a) Glass beads φ_p=0.051 (b) Glass beads φ_p=0.56

Figure 4. Instant fields of solid phase fraction, fluctuating kinetic energy, and velocity in the fluidized bed for glass beads (a) dilute regime (b) concentrated regime.

frequency and amplitude and tends to saturate in the upper part of the bed. This remarkable structure is very similar to the planar concentration cnoidal waves experimentally first analyzed by Nicolas et al.[6] and then by Duru et al.[8] In Figure 8, it can be also observed that the planar wave results from the transverse growth of "void fraction" instabilities that appears in the lower part of the bed. When their size reaches the column diameter (by growth or coalescence with others), they form "rectangular" bands that rise along the bed with a rectilinear motion, as shown on the corresponding velocity field (Figure 5b).

What is remarkable is that such a periodical one-dimensional (1D) structure is a peculiar solution of the 2D unsteady statistical model of this study. In some way, it is the opposite approach to that of Nicolas et al.[6] and Duru et al.[8] who developed constitutive closure laws of the solid phase rheology on the basis of the analytic form of the experimental solid phase fraction time signal. Their method can be summarized as follows: the analytic form of the saturated wave resulting from a forced wavy regime around the most energetic natural mode is implemented in a 1D two-fluid model (of same kind as that proposed by Anderson and Jackson[11]), which allowed them to identify the granular pressure (or the elasticity, its derivative with respect to the solid fraction) and the granular viscosity (shear viscosity). The scaling laws they obtain read:

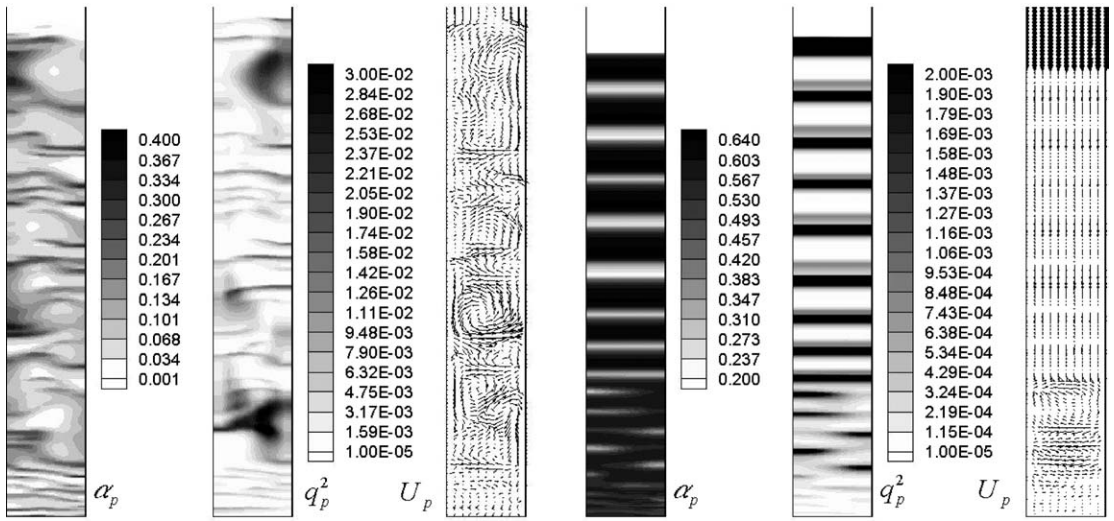

(a) Steel beads φ_p=0.11 (b) Steel beads φ_p=0.52

Figure 5. Instant fields of solid phase fraction, fluctuating kinetic energy, and velocity in the fluidized bed for steel beads (a) dilute regime (b) concentrated regime.

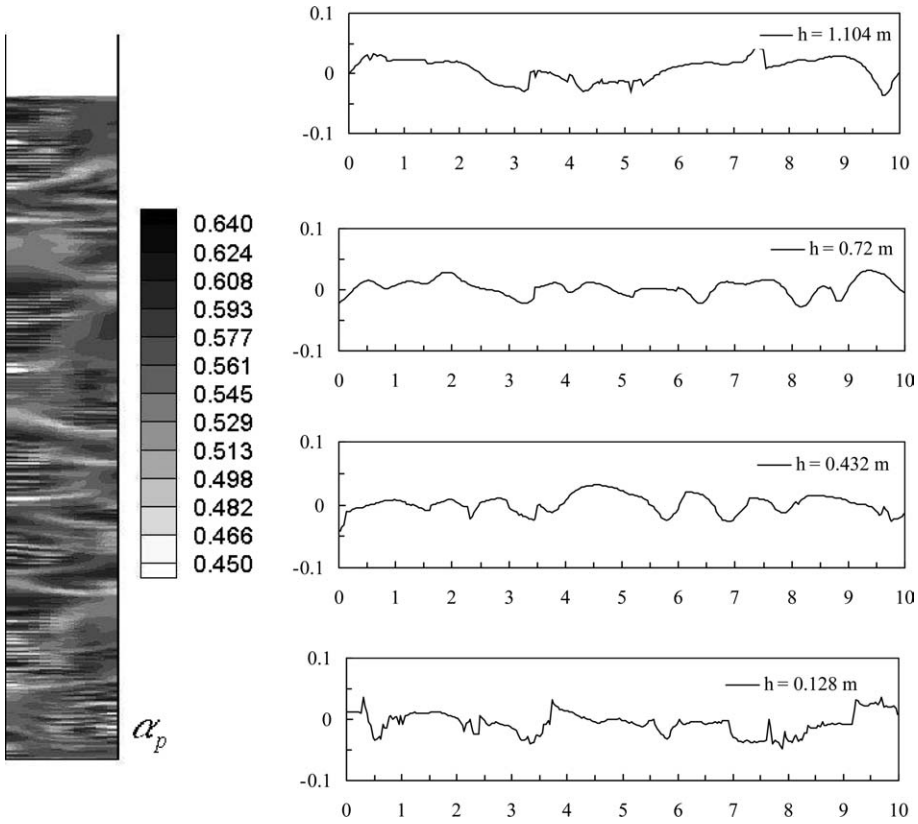

Figure 6. Axial evolution of the solid fraction fluctuation instant signal $\langle \alpha_p \rangle_S - \langle \overline{\alpha_p} \rangle_S$ in the bed cross section for Nylon beads and $\varphi_p = 0.56$.

Horizontal axis: time in seconds.

$$\mu_p^* = \frac{\mu_p}{\rho_p d U_t} = \frac{0.18}{\varphi_{rlp} - \varphi_p} \tag{14}$$

for the granular viscosity, where φ_{rlp} in an empirical maximum random packing fraction slightly smaller than $\varphi_{p,m}$. For the elasticity they find:

$$\frac{dP_p^*}{d\varphi_p} = \frac{1}{\rho_p U_t^2}\left(\frac{dP_p}{d\varphi_p}\right) = 0.2 \tag{15}$$

Note, however, that for the determination of the granular pressure, the results of Duru et al.[8] are rather sensitive to the available accuracy on the wave shape, in particular to the level of wave saturation. Comparison between the above scaling laws and the values predicted by the present model have been reported in Figure 9 for the granular viscosity and in Figure 10 for the normalized elasticity (using steel beads numerical data). In Figure 9, it can be seen that the reduced viscosity (inverse of a "granular" Reynolds number) is a decreasing function of $(\varphi_{p,m} - \varphi_p)$. The evolution of this normalized viscosity calculated by the model underestimates the law identified by Duru et al. by an order of magnitude and its slope is larger. Because of the important weight of the collisional viscosity at high phase fraction in the model,[26] such a discrepancy might be due to the formulation of the time between two collisions, τ_p^c which is a "dry granular" expression disregarding the effect of the interstitial fluid (Eq. 9).

The level of the reduced elasticity as a function of φ_p predicted by the model is approximately twice smaller than the value deduced from the experimental results of Duru et al.[8] It is thought that this difference comes from the fact that Eq. 15 results from an equilibrium between inertia and granular elasticity. In their 1D model, Duru et al. accounts for the added mass contribution in the inertia as it was ignored in the present simulation. At high concentration, the ratio between inertia terms with and without this added mass term is close to 2, explaining to a certain extent the difference. Moreover, Eq. 15 does not account for the stiff decrease of granular pressure experimentally observed in the neighborhood of φ_{rlp} and approximately represented in Figure 10 by the dashed line. It is worth to note that the model reproduces such behavior. Overall, considering the large magnitude of the experimental error bars (not reproduced here) around this variable, the agreement can be judged satisfactory.

Spectral analysis

The power spectrum of the particle concentration fluctuations has been calculated from the simulations at different sections along the bed height and compared with the experimental data of Zenit and Hunt.[28] Results are displayed in Figures 11–14 for the nylon beads and in Figures 15–18 for the steel beads. With both types of beads, dilute and concentrated cases have been represented and a sample of the corresponding time signal of the concentration fluctuation has been also reported. The sampling frequency of the numerical

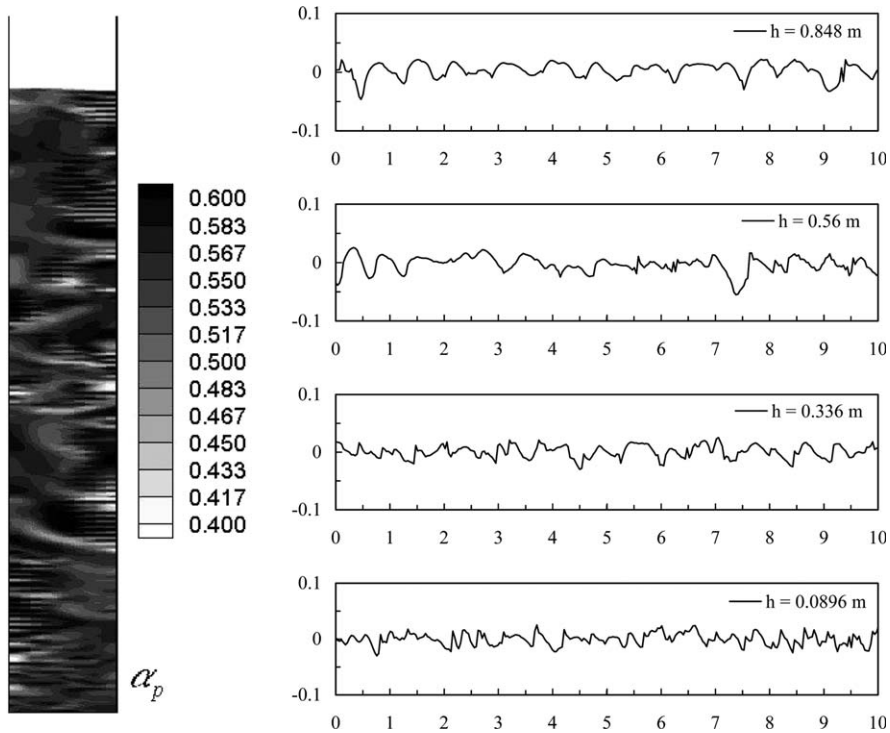

Figure 7. Axial evolution of the solid fraction fluctuation instant signal $\langle \alpha_p \rangle_S - \langle \overline{\alpha_p} \rangle_S$ in the bed cross section for glass beads and $\varphi_p = 0.56$.

Horizontal axis: time in seconds.

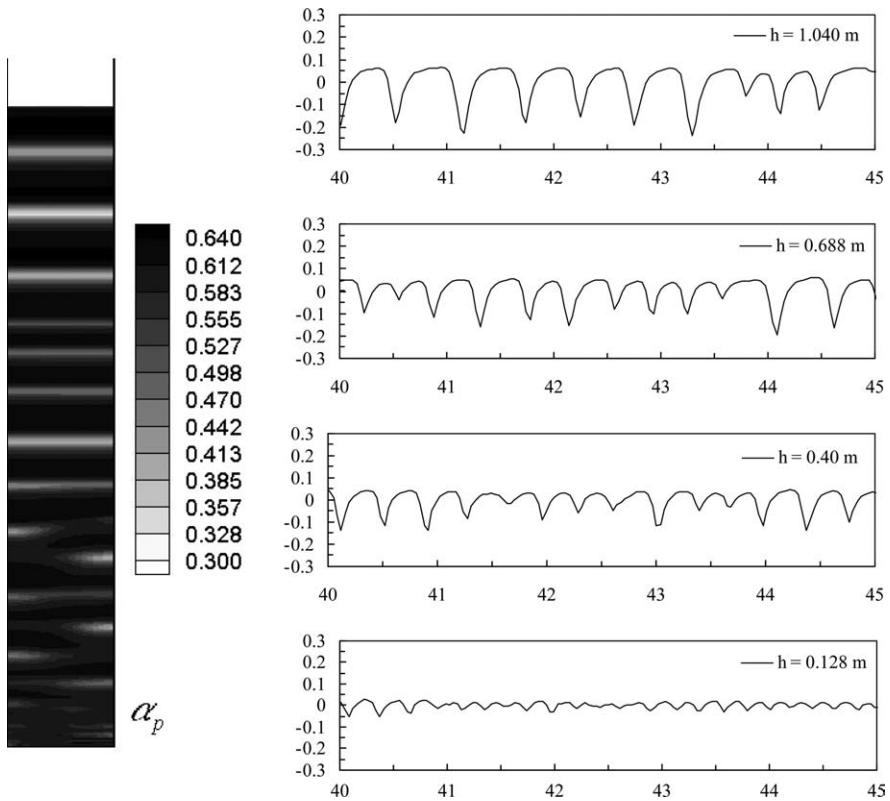

Figure 8. Axial evolution of the solid fraction fluctuation instant signal $\langle \alpha_p \rangle_S - \langle \overline{\alpha_p} \rangle_S$ in the bed cross section for steel beads and $\varphi_p = 0.60$.

Horizontal axis: time in seconds.

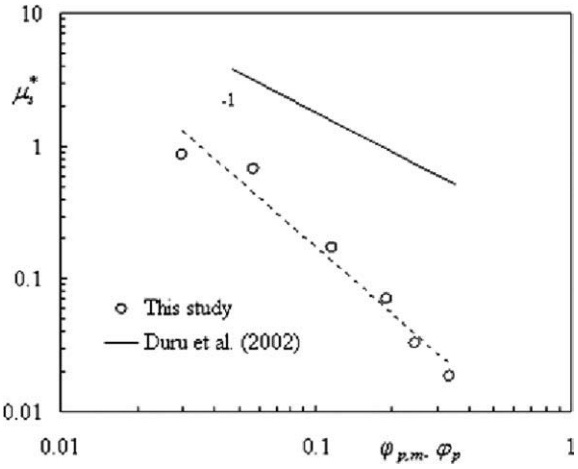

Figure 9. Reduced granular viscosity as a function of $\varphi_{p,m} - \varphi_p$.

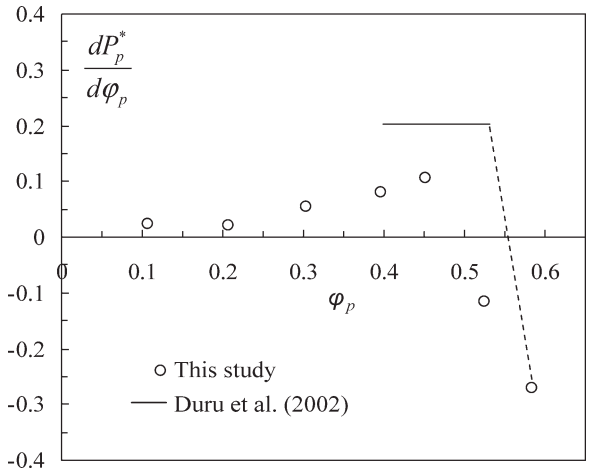

Figure 10. Reduced elasticity as a function of φ_p.

Straight lines represents the data of Duru et al. (2002); circles represent numerical simulations.

results is 28 Hz and the record length varies between 5000 and 2500 values depending on the global solid fraction. Spectrums are calculated by blocks of 256 values (each of them represents 9.2 s). Such an averaging process allows smoothing the spectrum in the range (0.1–14 Hz). The frequency spectrum and the amplitude of the solid fraction signal are varying along the bed height. For each case presented, the results correspond to the fluctuating signal of the cross-section averaged solid fraction in the upper part of the bed.

The case of the nylon beads at a low concentration ($\varphi_p = 0.11$) is shown in Figure 11. The simulated time signal (Figure 11b) exhibits positive peaks of amplitude at a characteristic frequency close to 1 Hz. This frequency corresponds to the passage of aggregate-like structures in the dilute regime (see also Figure 3a). For larger frequency, the calculated power density (Figure 12b) monotonously decays as a (-3) power law. Such a value of the slope suggests some

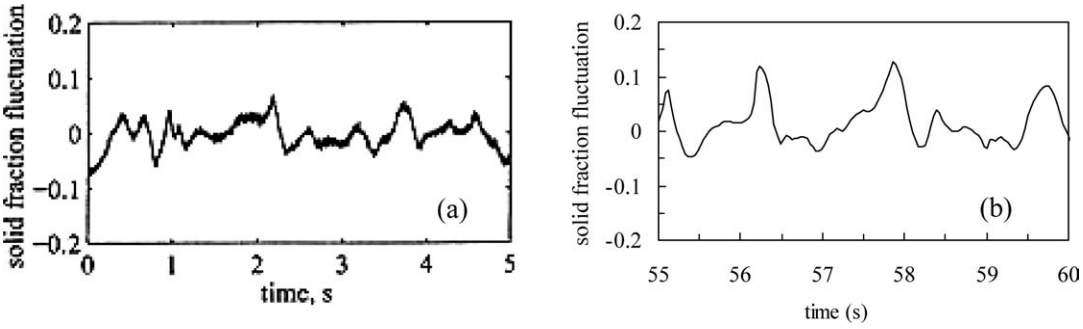

Figure 11. Solid fraction fluctuations $\varphi_p = 0.11$ (nylon beads).

(a) Experiments (b) Numerical.

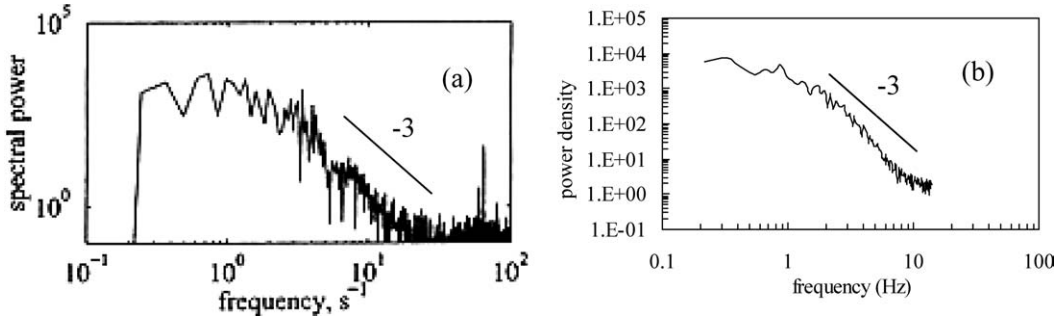

Figure 12. Solid fraction power spectrum $\varphi_p = 0.11$ (nylon beads).

(a) Experiments (b) Numerical.

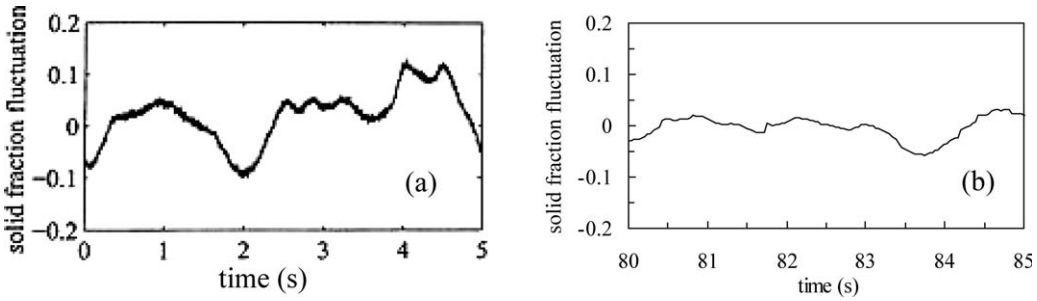

Figure 13. Solid fraction fluctuations $\varphi_p = 0.56$ (nylon beads).
(a) Experiments (b) Numerical.

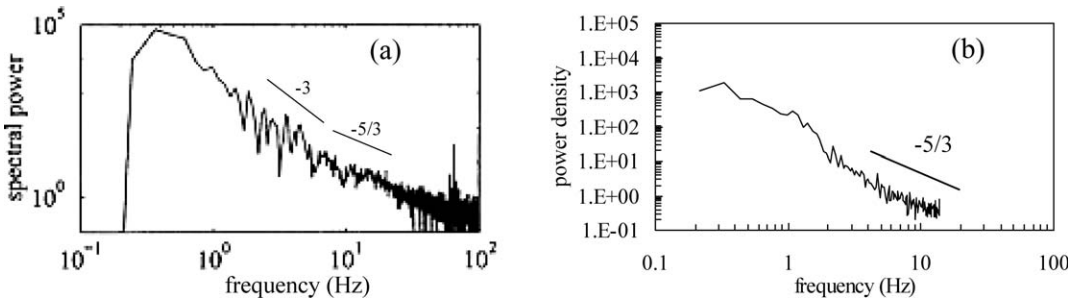

Figure 14. Solid fraction power spectrum $\varphi_p = 0.56$ (nylon beads).
(a) Experiments (b) Numerical.

similarity with the coupling of a turbulent spectrum with an external forcing.[33] In this case, the variation of power density is monitored by a single characteristic time scale over the whole frequency range. Conservation of energy, therefore, naturally implies a (−3) power decay as a function of frequency. Such a spectrum could be interpreted as the signature of the convolution of a quasi periodical signal (aggregate frequency) with the random motion of the dispersed

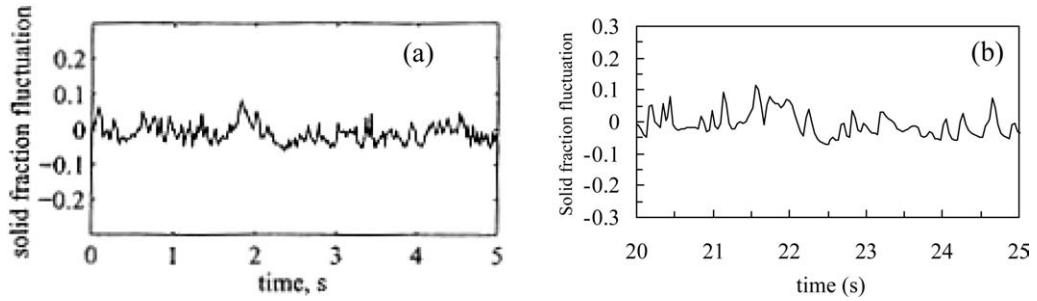

Figure 15. Solid fraction fluctuations $\varphi_p = 0.11$ (steel beads).
(a) Experiments (b) Numerical.

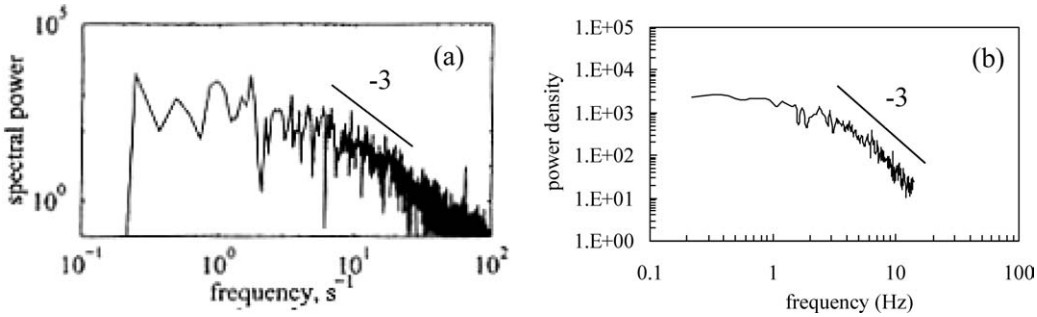

Figure 16. Solid fraction power spectrum $\varphi_p = 0.11$ (steel beads).
(a) Experiments (b) Numerical.

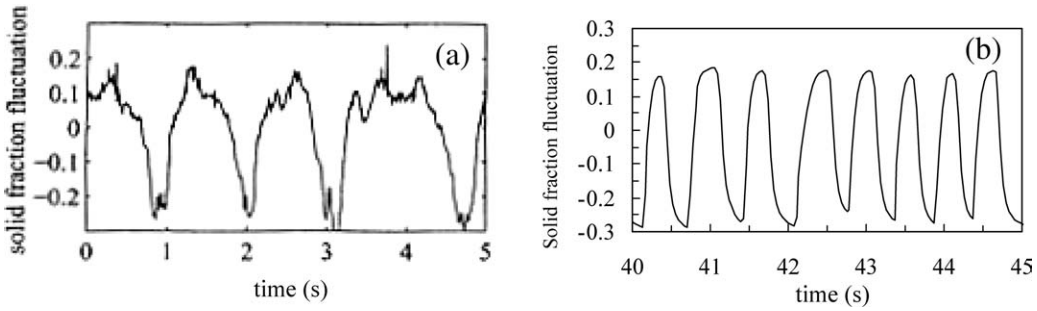

Figure 17. Solid fraction fluctuations $\varphi_p = 0.47$ for steel beads.
(a) Experiments (b) Numerical.

phase. The experimental time signal (Figure 11a) presents similar positive peaks and despite the high noise level on the experimental spectrum (Figure 12a), its amplitude and shape resemble the numerical spectrum.

In the case of the nylon beads at high concentration, the numerical time signal is significantly changed, which is characterized by the presence of negative low-frequency fluctuations (Figure 13b). There is no real dominant frequency of these fluctuations that seem to be more continuously distributed over several low-frequency modes. The corresponding power density is reported in Figure 14b and its variation at higher frequency is close to a (−5/3) power decay (random "turbulent" motion of the particles). When compared with the experimental signal (Figure 13a), the numerical signal amplitude is weaker. The experimental signal (Figure 13a) also possesses these low frequency "void fraction" peaks (negative fluctuations) but in this case, the existence of a high energy dominant mode (around 0.5 Hz) is observed. As a result, the experimental spectrum energy at low frequency is much higher than that of numerically observed (nearly 2 orders of magnitude) and exhibits a (−3) power decay behavior prior to the −5/3 at high frequency (Figure 14a).

The case of the most inertial particles (steel beads) at low concentration is reported in Figure 15. The amplitude of the time signal is smaller than with the nylon beads and its fluctuations have larger frequencies. Experimental (Figure 15a) and numerical (Figure 15b) signals possess similar trends. The corresponding spectrums in Figures 16a, b (experimental and numerical) exhibit a (−3) slope, suggesting the existence of a dominant frequency. It seems that this frequency is ranging between 2 and 3 Hz in the numerical signal but is difficult to identify in the experimental signal (because of the high noise level).

At high concentration and in the case of the steel beads, a low-frequency quasi periodical signal of high negative amplitude develops along the bed, which characterizes the occurrence of the aforementioned "planar concentration waves" (Figure 17). The dominant mode of the numerical signal is located around 1.8 Hz, as shown in Figure 17b. The similarity with the experimental signal is remarkable (Figure 17a) but the experimental frequency is approximately twice less as that predicted by the model (0.9 Hz).

Such results confirm the relevance of the present approach to describe the dynamics of liquid fluidization but also the differences between the granular viscosity and elasticity as predicted by the model and the experimental findings of Duru et al.[8] Because of the strong nonlinear coupling between the momentum and the fluctuating kinetic transport, it is still difficult to identify and predict the specific effect of the granular pressure and viscosity on the intensity and distribution of the solid fraction power spectrum.

Solid fraction rms

To complete this study, the experimental and numerical values of the solid phase fraction rms $\sqrt{\langle \overline{\alpha_p'^2} \rangle}$ have been compared (which is also equal to the power density integral over the whole frequency domain). The experimental data show that, at a given concentration, the mean level of this value is approximately of same order of magnitude for all beads except for the steal beads at high concentration. The

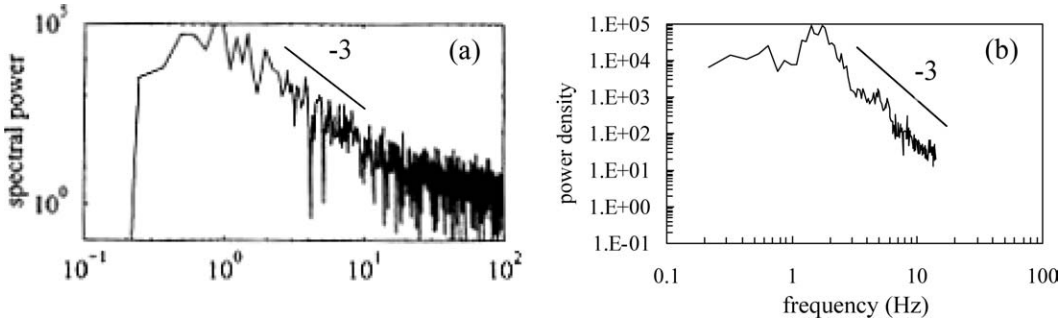

Figure 18. Solid fraction power spectrum $\varphi_p = 0.47$ for steel beads.
(a) Experiments (b) Numerical.

evolution of the solid fraction rms has been plotted as a function of the mean solid fraction in Figure 19 for the three types of beads. In dilute regime, the experimental rms (crosses) is an increasing function of the concentration and a stiff decreasing function at highest concentration (in the neighborhood of $\varphi_{p,m}$). Such an evolution is consistent with the granular pressure or temperature variation with the solid fraction and can be predicted on the basis of simple considerations. The fluidization velocity is related to the global concentration by the Richardson–Zaki equation (Eq. 12). Expressed in terms of average continuous phase velocity U_f, it reads:

$$U_f = U_t(1-\varphi_p)^{n-1} \tag{16}$$

Assuming this macroscopic relation to be valid at a local scale, the liquid phase velocity fluctuation u'_f can thus be related to the solid fraction fluctuation α'_p as follows:

$$u'_f \approx \frac{dU_f}{d\varphi_p}\alpha'_p = -U_t(n-1)(1-\varphi_p)^{n-2}\alpha'_p \tag{17}$$

In the range of Stokes number considered and for solid phase fraction larger than 0.1, one may also admit that the continuous phase and particle velocity fluctuations are strongly correlated, leading to the following relation between the fluctuating kinetic energy of the solids and the rms of the solid phase fraction:

$$\sqrt{\left\langle \overline{\alpha'^2_p} \right\rangle} \approx \frac{2\sqrt{\left\langle \overline{q^2_p} \right\rangle}}{3(n-1)U_t(1-\varphi_p)^{n-2}} \tag{18}$$

Substituting Eq. 13 in the above relation provides a scaling relation of the solid phase fraction rms and the mean concentration:

$$\sqrt{\left\langle \overline{\alpha'^2_p} \right\rangle} \propto \frac{2\left[C_{D0}\varphi_p(1-\varphi_p)^{-4.7}\right]^{1/3}(1-\varphi_p/\varphi_{p,m})^{n\varphi_{p,m}}}{3(n-1)(1-\varphi_p)^{n-2}} \tag{19}$$

At high particle Reynolds number, the drag coefficient of a single particle C_{D0} is close to 0.43 and is a slight function of Re_p. The term $C_{D0}^{1/3}$ can thus be considered as a constant in Eq. 19 (except at low fluidization velocity or equivalently in the neighborhood of the maximum packing solid fraction). As a result, at a given concentration φ_p, the rms of the solid phase fraction of each type of beads mainly depends of the scaling factor in the fluctuating kinetic energy correlation (Eq. 13), equal to 0.025, 0.028, and 0.06 for the nylon, glass, and steel beads, respectively. This approximation of the scaling of $\sqrt{\left\langle \overline{\alpha'^2_p} \right\rangle}$ explains the low dependence of $\sqrt{\left\langle \overline{\alpha'^2_p} \right\rangle}$ on the beads inertia. The solid fraction rms as predicted by Eq. 19 has been plotted in Figure 19 for the three types of beads (open circles) and shows a reasonable agreement with experimental results in a wide range of solid phase fraction.

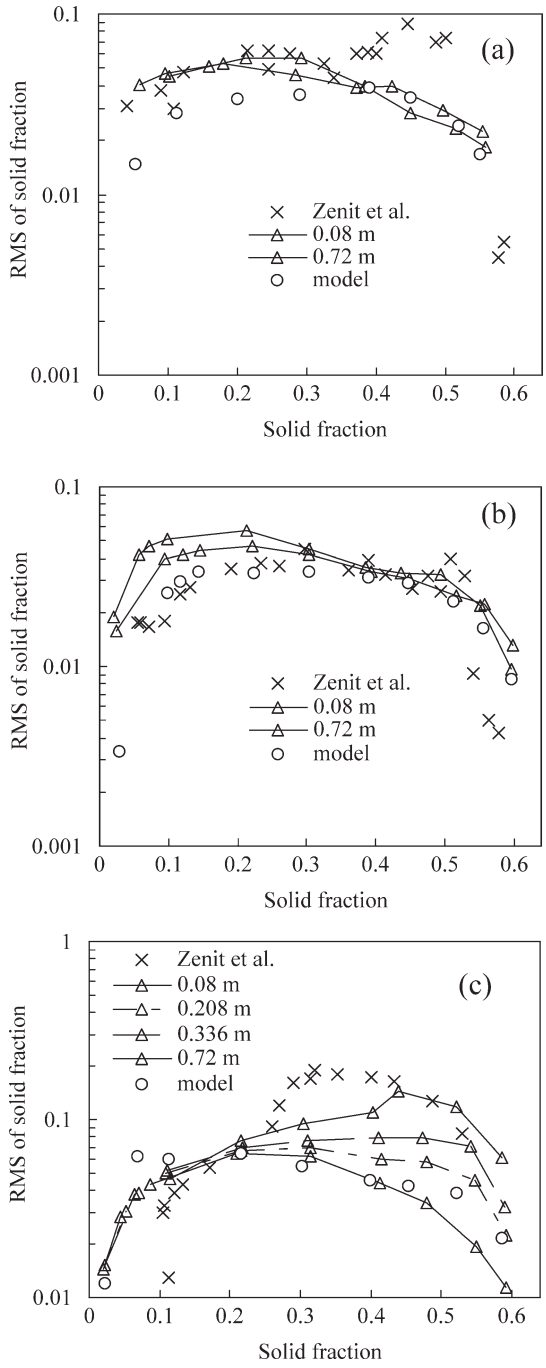

Figure 19. RMS of solid fraction as a function of φ_p. (a) nylon beads (b) glass beads (c) steel beads.

Symbols: crosses, experimental data of Zenit et al.; triangles, numerical data at different sections along the bed; circles, Eq. 19.

Because of the approximation of Eq. 17, Eq. 19 is, however, limited to the case of a homogeneous flow configuration, despite the fact that the expression of the averaged fluctuating kinetic energy used in that model partly accounts for large scale motion.

The "bump" observed in these graphs for the three types of beads at high concentration is due to the occurrence of low frequency "void fraction" single mode waves

developing along the bed height. Hence, this "bump" is more pronounced with high inertia particles (Figure 19c, steel beads) than with low and moderate inertia particles (Figures 19a, b, nylon and glass beads, respectively). However, it must be noted that this bump is more pronounced in the case of the nylon beads than with the glass beads, suggesting an attenuation of the concentration wave in the case of the glass beads. Such an effect might be due to a too large value of the ratio D/d between the column diameter (5 cm) and the glass particle diameter (3 mm). The numerical predictions have been also plotted in these graphs at different sections along the bed (triangles). In all cases, these are in fairly good agreement with the experimental values except for the reproduction of the bump in the range $0.4 < \varphi_p < 0.5$, as expected from the former spectral analysis. In the case of the steel beads, the agreement is still quite acceptable and in this case, the numerical values "measured" at the top of the bed (Figure 19c, $z = 0.72$ m) tend to better reproduce the experimental trend, except in the range $0.3 < \varphi_p < 0.4$ where they still underestimate the experimental values. Note that in this case, the simplified model cannot well represent the measured evolution at high phase fraction due to approximation of Eq. 17.

Conclusions

A statistical model based on kinetic theory of granular flows has been applied to the description of solid–liquid fluidization.[26] In this work, we have focused our analysis on the unsteady structures as predicted by this model and compared them with the experimental data of Zenit and Hunt[29] and Duru et al.[8] Three kinds of contrasted inertia beads fluidized by water in a 5.1 cm diameter column have been selected for the 2D simulation test cases. For every type of bead, calculations were performed in a wide range of global solid phase fraction (from dilute to highly concentrated beds). In most of the cases, the large scale instantaneous structures calculated by the model result from the establishment of a series of contra-rotating circulation loops within which particles distribute in concentric zones. The center of these zones corresponds to a deficit in particles and the periphery to an excess of particles (with respect to the mean solid fraction). These rotational structures are responsible of the production of the fluctuating (small scale) kinetic energy of the dispersed phase. In the particular case of heavy particles (steel beads) at high concentration, the model predicts the development of single mode concentration planar waves. Their amplitude grows and frequency decreases from the bottom to the top of the bed and these waves tend to saturate at a given height. These well-organized structures developing on the whole width of the bed do well when compared with previous observations in the literature. In this case, the rotational structures disappear to the benefit of a 1D compressible flow, and the production terms of the small scale fluctuations are controlled by the granular pressure and the volume viscosity. The comparison of the granular shear viscosity and elasticity predicted by the model with the experimental data of Duru et al. reveal similar trends but these two variables seem to be underestimated by the present model. Spectral analysis of solid fraction large scale fluctuations have shown the existence of amplitude maxima at low frequency (of the order of 1 Hz) in dilute regimes (aggregate structures) as in concentrated regimes ("void fraction waves"). The occurrence of a low-frequency natural forcing in the signal is also supported by the presence of (-3) slope at higher frequency. At high concentration, the development of "void fraction" waves is more attenuated with the model than with the experiments. The analysis of solid fraction rms has confirmed the trends observed in the spectrum. Overall, the level of prediction of the present model can be judged quite satisfactory and calls for further developments. Thanks to the progress of the computing resources and the numerical techniques, direct numerical simulations offer promising perspectives for dispersed flow predictions but are still limited in domain size and particle concentration.[34] In return, DNS can be used to establish and validate the dispersed phase rheology as described in the statistical model (granular pressure and viscosity, collision frequency, etc.). Such a work is currently under progress.

Acknowledgments

This work was supported by the French Ministry of Education and Research and by the Centre National de la Recherche Scientifique (CNRS). The authors are also grateful to the research federation FER-MaT for financial support.

Notation

C_D = drag coefficient
C_{D0} = single particle drag coefficient
d = particle diameter (m)
D = fluidized bed diameter (m)
e_c = normal coefficient of restitution of collisions
g_0 = pair distribution function
$\mathbf{I}$ = unit tensor
K_p^{kin} = kinetic diffusivity ($m^2\ s^{-1}$)
K_p^{col} = collisional diffusivity ($m^2\ s^{-1}$)
n = exponent in Richardson–Zaki law
pdf = probability density function
P_p = granular pressure (Pa)
P_g^* = reduced granular pressure
q_p^2 = fluctuating kinetic energy of the solid phase ($m^2\ s^{-2}$)
Re = particle Reynolds number in the fluidized bed
Re_t = particle Reynolds number at terminal velocity
rms = root mean square
t = time (s)
T_{fp}^F = drag induced particle relaxation time (s)
U_0 = axial fluidization velocity ($m\ s^{-1}$)
$\mathbf{U}_p$ = local velocity vector of the solid phase ($m\ s^{-1}$)
U_t = particle terminal velocity ($m\ s^{-1}$)
u_r = local slip velocity ($m\ s^{-1}$)
U_f = axial component of fluid velocity ($m\ s^{-1}$)
u_f' = local fluid velocity fluctuation ($m\ s^{-1}$)
x_i = spatial coordinate in the ith direction (m)

Greek letters

α_p = local solid phase fraction
α'_p = local solid phase fraction fluctuation
$\varphi_p = \left(\sqrt{\langle \overline{\alpha_p'^2} \rangle}\right)$ global solid phase fraction
ϕ_c, σ_c = scalar function of e_c
λ_p = volume viscosity (Pa s)
μ_p = granular shear viscosity (Pa s)
μ^*s = dimensionless granular shear viscosity
ν_f = fluid viscosity ($m^2\ s^{-1}$)
ν_p^{kin} = kinetic viscosity ($m^2\ s^{-1}$)
ν_p^{col} = collisional viscosity ($m^2\ s^{-1}$)
ρ_f = fluid density ($kg\ m^{-3}$)

ρ_p = particle density (kg m^{-3})
Σ_p = stress tensor of the solid phase (Pa)
τ_p^c = time between two successive collisions (s)

Subscripts

i,j = coordinate indices
p = particle (solid) phase
p,m = maximum packing
f = (fluid phase)
rlp = random loose packing

Symbols

$\langle\psi\rangle$ = volume average in the bed
$\langle\psi\rangle_S$ = section average in the bed
$\bar{\psi}$ = time average (over all time scales)

Literature Cited

1. Epstein N. Applications of liquid–solid fluidization. *Int J Chem React Eng*. 2003;1:1–16.
2. Buffière P, Moletta R. Collision frequency and collisional particle pressure in three-phase fluidized beds. *Chem Eng Sci*. 2000;55: 5555–5563.
3. Di Felice R. Hydrodynamics of liquid fluidisation. *Chem Eng Sci*. 1995;50:1213–1245.
4. Didwania AK, Homsy GM. Flow regime and flow transitions in liquid-fluidized beds. *Int J Multiphase Flow*. 1981;7:563–580.
5. El-Kaissy MM, Homsy GM. Instability waves and the origin of bubbles in fluidized beds. Part I. Comparison with theory. *Int J Multiphase Flow*. 1976;6:305–318.
6. Nicolas M, Chomaz JM, Vallet D, Guazzelli E. Experimental investigations on the nature of the first wavy instability in liquid-fluidized beds. *Phys Fluids*. 1996;8:1987–1989.
7. Nicolas M, Hinch J, Guazzelli E. Wavy instability in liquid fluidized beds. *Ind Eng Chem Res*. 1999;38:779–802.
8. Duru P, Nicolas M, Hinch J, Guazzelli E. Constitutive laws in liquid-fluidized beds. *J Fluid Mech*. 2002;452:371–404.
9. Jackson R. The mechanics of fluidized beds. Part I. The stability of the state of uniform fluidization. *Trans Inst Chem Eng*. 1963;41:13–21.
10. Murray JD. On the mathematics of fluidization. Part I. Fundamental equations and wave propagation. *J Fluid Mech*. 1965;21:465–493.
11. Anderson TB, Jackson R. Fluid mechanical description of fluidized beds. Equations of motion. *I&EC Fund*. 1967;6:527–539.
12. Lun CKK, Savage SB, Jefferey DJ, Chepurniy N. Kinetic theory for granular flow: inelastic particles in couette flow and slightly inelastic particles in a general flow field. *J Fluid Mech*. 1984;140:223–256.
13. Balzer G, Boelle A, Simonin O. Eulerian gas–solid flow modeling of dense fluidized bed, fluidisation VIII. Fluidization VIII, proceedings of the 8th Engineering Foundation Conference on Fluidization, May 14–19, 1995, Tours, France, edited by Jean-François Large and Claude Laguérie. Engineering Foundation, New York, 1996.
14. Batchelor GK. A new theory of the instability of a uniform fluidized bed. *J Fluid Mech*. 1988;193:75–110.
15. Anderson K, Sundaresan S, Jackson R. Instabilities and the formation of bubbles in fluidized beds. *J Fluid Mech*. 1995;303:327–366.
16. Jenkins JT, Richmann MW. Kinetic theory for plane flows of a dense gas of identical, rough, inelastic, circular disks. *Phys Fluids*. 1985;28:3485–3494.
17. Chapman S, Cowling TG. *The Mathematical Theory of Non-Uniform Gases*. Cambridge: Cambridge Mathematical Library, 1970.
18. Koch DL. Kinetic theory for a monodisperse gas–solid suspension. *Phys Fluids A*. 1990;2:1711–1723.
19. Ma D, Ahmadi G. A kinetic model for rapid granular flows of nearly elastic particles including interstitial fluid effects. *Powder Technol*. 1988;56:191–207.
20. Ding J, Gidaspow D. A bubbling fluidization model using kinetic theory of granular flow. *AIChE J*. 1990;36:523–538.
21. Boelle A, Balzer G, Simonin O. Second-order prediction of the particle-phase stress tensor of inelastic spheres in simple shear dense suspensions. *Gas-Solid Flows ASME FED*. 1995;228:9–18.
22. Simonin O. Prediction of the dispersed phase turbulence in particle-laden jets. *Gas-Solid Flows ASME FED*. 1991;121:197–206.
23. Simonin O. Statistical and Continuum Modelling of Turbulent Reactive Particulate Flows. Part I. Theoretical Derivation of Dispersed Eulerian Modelling from Probability Density Function Kinetic Equation. Theoretical and Experimental Modeling of Particulate Flows, Lecture Series 2000–06. *Rhode Saint Genèse (Belgium)*: *von Karman Institute for Fluid Dynamics*, 2000.
24. Gobin A, Neau H, Simonin O, Llinas JR, Reiling V, Selo JL. Fluid dynamic numerical simulation of a gas phase polymerisation reactor. *Int J Numer Methods Fluids*. 2003;43:1199–1220.
25. Vermorel O, Bedat B, Simonin O, Poinsot T. Numerical study and modelling of turbulence modulation in a particle laden slab flow. *J Turbulence*. 2003;25:1–39.
26. Gevrin F, Masbernat O, Simonin O. Granular pressure and particle velocity fluctuation predictions in liquid fluidized beds. *Chem Eng Sci*. 2008;63:2450–2464.
27. Gevrin F, Masbernat O, Simonin O. ICMF'04, Y Matsumoto, K Hishida, A Tomiyama, K Mishima and S Hosokawa (Eds.), 2004; paper n: 455 Numerical study of solid–liquid fluidization dynamics. In: *Proceedings of ICMF'04*. Yokohama, Japan, 2004.
28. Zenit R, Hunt ML, Brennen CE. Collisional particle pressure measurements in solid-liquid flows. *J Fluid Mech*. 1997;353:261–283.
29. Zenit R, Hunt ML. Solid fraction fluctuations in solid–liquid flows. *Int J Multiphase Flow*. 2000;26:763–781.
30. Lun CKK, Savage SB. The effect of an impact velocity dependent coefficient of restitution on stresses developed by sheared granular material. *Acta Mechanica*. 1986;63:14–44.
31. Wen CY, Yu YH. Mechanics of fluidization, *Chem Eng Symp Ser*. 1966;62:100–111.
32. Clift R, Grace JR, Weber ME. *Bubbles, Drops and Particles*. New York: Academic Press, 1978.
33. Thais L, Magnaudet J. Turbulent structure beneath surface gravity waves sheared by the wind. *J Fluid Mech*. 1996;328:313–344.
34. Climent E, Maxey MR. Numerical simulation of random suspensions at finite Reynolds numbers. *Int J Multiphase Flow*. 2003;29: 579–601.

Manuscript received Jan. 23, 2008, revision received Sept. 24, 2009, and final revision received Feb. 10, 2010.